Research Article | Vol. 25, No. 8 | 17 Apr 2017 | OPTICS EXPRESS 8534

Optics EXPRESS

Electrifying catheters with light

MARTIN PEKAŘ,[1,2*] JEANNET VAN RENS,[1] AND MARTIN B. VAN DER MARK[1]

[1] *Philips Research, Royal Philips NV, High Tech Campus 34, 5656 AE Eindhoven, Netherlands*
[2] *Erasmus MC, Thorax Center Department of Biomedical Engineering, Wytemaweg 80, 3015 CN Rotterdam, Netherlands*
[*] *martin.pekar@philips.com*

Abstract: Smart minimally invasive devices face a connectivity challenge. An example is found in intracardiac echocardiography where the signal transmission and supply of power at the distal end require many thin and fragile wires in order to keep the catheter slim and flexible. We have built a fully functional bench-top prototype to demonstrate that electrical wires may be replaced by optical fibers. The prototype is immediately scalable to catheter dimensions. The absence of conductors will provide intrinsic galvanic isolation as well as radio frequency (RF) and magnetic resonance imaging (MRI) compatibility. Using optical fibers, we show signal transfer of synthetic aperture ultrasound images as well as photo-voltaic conversion to supply all electronics. The simple design utilizes only off the shelf components and holds a promise of cost effectiveness which may be pivotal for translation of these advanced devices into the clinic.

OCIS codes: (060.2330) Fiber optics communications; (230.2090) Electro-optical devices; (170.7170) Ultrasound.

References and links

1. D. M. Cosgrove and J. F. Sabik, "Minimally invasive approach for aortic valve operations," Ann. Thorac. Surg. **62**, 596–597 (1996).
2. J. L. Navia and D. M. Cosgrove, "Minimally invasive mitral valve operations," Ann. Thorac. Surg. **62**, 1542–1544 (1996).
3. N. Baltayiannis, C. Michail, G. Lazaridis, D. Anagnostopoulos, S. Baka, I. Mpoukovinas, V. Karavasilis, S. Lampaki, A. Papaiwannou, A. Karavergou, I. Kioumis, G. Pitsiou, N. Katsikogiannis, K. Tsakiridis, A. Rapti, G. Trakada, A. Zissimopoulos, K. Zarogoulidis, and P. Zarogoulidis, and Others, "Minimally invasive procedures," Ann. Transl. Med. **3**, 55 (2015).
4. I. Gonzalez, Q. Cao, and Z. Hijazi, "Role of Intracardiac Echocardiography (ICE) in Transcatheter Occlusion of Atrial Septal Defects," in *Atrial Septal Defect*, P. S. Rao, ed. (InTech, 2012), pp. 99–118.
5. T. Bartel, N. Bonaros, L. Müller, G. Friedrich, M. Grimm, C. Velik-Salchner, G. Feuchtner, F. Pedross, and S. Müller, "Intracardiac echocardiography: a new guiding tool for transcatheter aortic valve replacement," J. Am. Soc. Echocardiogr. **24**, 966–9575 (2011).
6. Z. M. Hijazi, K. Shivkumar, and D. J. Sahn, "Intracardiac echocardiography during interventional and electrophysiological cardiac catheterization," Circulation **119**, 587–96 (2009).
7. K. Ratnayaka, A. Z. Faranesh, M. S. Hansen, A. M. Stine, M. Halabi, I. M. Barbash, W. H. Schenke, V. J. Wright, L. P. Grant, P. Kellman, O. Kocaturk, and R. J. Lederman, "Real-time MRI-guided right heart catheterization in adults using passive catheters," Eur. Heart J. **34**, 380–388 (2013).
8. R. Razavi, D. L. G. Hill, S. F. Keevil, M. E. Miquel, V. Muthurangu, S. Hegde, K. Rhode, M. Barnett, J. Van Vaals, D. J. Hawkes, and E. Baker, "Cardiac catheterisation guided by MRI in children and adults with congenital heart disease," Lancet **362**, 1877–1882 (2003).
9. F. L. Degertekin, C. Tekes, L. R. Jay, O. Kocaturk, M. W. Rashid, and M. Ghovanloo, "MRI Compatible 3-D Intracardiac Echography Catheter and System," Patent WO2015048321 (A1) (2015).
10. M. Konings, S. Weiss, and C. Bakker, "Catheters and guidewires in interventional MRI: problems and solutions," MedicaMundi **45**, 31–39 (2001).
11. M. K. Konings, L. W. Bartels, H. F. M. Smits, and C. J. G. Bakker, "Heating around intravascular guidewires by resonating RF waves," J. Magn. Reson. Imaging **12**, 79–85 (2000).
12. A. Alduino and M. Paniccia, "Wiring electronics with light," Nature Photon. **1**, 153–155 (2007).
13. S. Fandrey, S. Weiss, and J. Müller, "A novel active MR probe using a miniaturized optical link for a 1.5-T MRI scanner," Magn. Reson. Med. **67**, 148–155 (2012).
14. M. Hofstetter, J. Howgate, M. Schmid, S. Schoell, M. Sachsenhauser, D. Adigüzel, M. Stutzmann, I. D. Sharp, and S. Thalhammer, "In vitro bio-functionality of gallium nitride sensors for radiation biophysics," Biochem. Biophys. Res. Commun. **424**, 348–353 (2012).

#285514 https://doi.org/10.1364/OE.25.008534
Journal © 2017 Received 23 Jan 2017; revised 21 Mar 2017; accepted 22 Mar 2017; published 3 Apr 2017

Optics EXPRESS

15. S. A. Jewett, M. S. Makowski, B. Andrews, M. J. Manfra, and A. Ivanisevic, "Gallium nitride is biocompatible and non-toxic before and after functionalization with peptides," Acta Biomaterialia **8**, 728–733 (2012).
16. A. S. Ergun, G. G. Yaralioglu, and B. T. Khuri-Yakub, "Capacitive Micromachined Ultrasonic Transducers: Theory and Technology," J. Aerospace Eng. **16**, 76–84 (2003).
17. J. H. Klootwijk, P. Dirksen, M. Mulder, and E. M. L. Moonen, "Capacitive Micromachine Ultrasound Transducer," Patent US2011163630 (A1) (2011).
18. M. Pekař, W. U. Dittmer, N. Mihajlović, G. van Soest, and N. de Jong, "Frequency Tuning of Collapse-Mode Capacitive Micromachined Ultrasonic Transducer," Ultrasonics **74**, 144–152 (2017).
19. K. L. Gammelmark and J. A. Jensen, "Multielement Synthetic Transmit Aperature Imaging Using Temporal Encoding," IEEE Trans. Med. Imaging **22**, 552–563 (2003).
20. I. Trots, A. Nowicki, M. Lewandowski, and Y. Tasinkevych, "Synthetic aperture method in ultrasound imaging," in *Ultrasound Imaging*, M. Tanabe, ed. (InTech, Rijeka, 2011), chap. 3, pp. 37–56.
21. M. B. van der Mark, A. van Dusschoten, and M. Pekař, "All-optical power and data transfer in catheters using an efficient LED," in *Optical Fibers and Sensors for Medical Diagnostics and Treatment Applications XV*, I. Gannot, ed. (SPIE Photonics West, San Francisco, 2015), 9317.
22. M. B. van der Mark and A. H. van Dusschoten, "An optical probe system," Patent US2015335231 (A1) (2015).
23. J. A. Jensen, "Field: A program for simulating ultrasound systems," Med, Biol. Eng. Comput. **34**, 351–353 (1996).
24. J. A. Jensen, "Ultrasound imaging and its modeling," in *Imaging of Complex Media with Acoustic and Seismic Waves*, vol. 84 (Springer, 2002), pp. 135–136.
25. M. A. Lediju, G. E. Trahey, B. C. Byram, and J. J. Dahl, "Short-lag spatial coherence of backscattered echoes: Imaging characteristics," IEEE Trans. Ultrason., Ferroelect., Freq. Control **58**, 1377–1388 (2011).
26. B. A. J. Angelsen, *Ultrasound Imaging: Waves, Signals, and Signal Processing Vol I* (Emantec, 2000).
27. I. Ladabaum, P. Wagner, C. Zanelli, J. Mould, P. Reynolds, and G. Wojcik, "Silicon substrate ringing in microfabricated ultrasonic transducers," in *Proceedings - IEEE Ultrasonics Symposium* (IEEE, 2000), pp. 943–946.
28. J. A. Jensen, S. I. Nikolov, K. L. Gammelmark, and M. H. Pedersen, "Synthetic aperture ultrasound imaging," Ultrasonics **44**, e5–e615 (2006).
29. W. C. Black, S. Member, and D. N. Stephens, "CMOS Chip for Invasive Ultrasound Imaging," IEEE J. Solid-State Circuits **29**, 1381–1387 (1994).
30. I. Ladabaum, X. Jin, H. T. Soh, A. Atalar, and B. T. Khuri-Yakub, "Surface micromachined capacitive ultrasonic transducers," IEEE Trans. Ultrason., Ferroelect., Freq. Control **45**, 678–90 (1998).
31. C. T. Leondes, ed., *MEMS/NEMS Handbook: Techniques and Applications* (Springer US, 2007).
32. P. Roriz, O. Frazão, A. B. Lobo-Ribeiro, J. L. Santos, and J. A. Simões, "Review of fiber-optic pressure sensors for biomedical and biomechanical applications," J. Biomed. Opt. **18**, 50903 (2013).
33. M. Karaman and M. O'Donnell, "Synthetic aperture imaging for small scale systems," IEEE Trans. Ultrason., Ferroelect., Freq. Control **42**, 429–442 (1995).

1. Introduction

Modern medicine aims to replace conventional diagnostic and therapeutic procedures with minimally invasive interventions [1–3]. Reduced trauma, shorter hospital stay and reduced costs are the most important drivers for the adoption of catheter-based invasive techniques. To increase the clinical value of minimally invasive tools (ie. catheters, guide wires, sheaths), navigational or therapeutic functionality is integrated at the tip of these devices. Smart sensors or actuators in the tip require integration of electrical supply power and signal transmission, which can be challenging, in particular when high data-rate channels, consisting of many electrical wires, are needed. The large aspect ratio of diameter and length of a guide wire or catheter severely limits the total number and diameter of electrical wires that can be integrated in such a device. The integration of wires compromises bending and stiffness, the key properties for steering of the instrument. Also, the metal wires severely challenge magnetic resonance imaging (MRI) compliance and radio frequency (RF) compatibility. Last but not least, extra measures are required regarding galvanic isolation, being of crucial importance for devices that come in an intimate contact with the patient.

Indeed, smart minimally invasive devices clearly face a connectivity challenge. An example is found in intracardiac echocardiography (ICE) which is a minimally-invasive procedure used to diagnose cardiovascular conditions and to provide navigation of other instruments inside the heart [4–6]. During cardiac catheterization, the catheter (a long thin tube) is inserted in an artery or vein in the groin, neck or arm and threaded through the blood vessels into the

Optics EXPRESS

heart. This is usually done under image guidance of X-ray fluoroscopy. Unfortunately, X-ray imaging technique provides poor soft-tissue contrast and generates ionizing radiation which is harmful to both the clinician and the patient. A lot of interest has grown in recent years in the use of real-time 2-D MRI which has proven to be safe and practical while enabling completely radiation-free navigation [7,8]. Apart from the navigation, 3-D real-time imaging of heart features and instruments is desired for a complex catheter-based cardiovascular treatments of structural heart diseases, which is difficult to achieve with the real-time MRI. Present state-of-the-art research is therefore focused on developing 3-D ICE that would be MRI safe, by replacing the conventional coaxial wires with its MRI-compatible version [9]. Metallic conductors longer than 10 cm, typically used in imaging catheters, are a potential hazard in the MRI environment [10]. The specific hazard comes from the resonance of the RF waves, which can cause temperature rise to as much as 74°C in 30s [11], but the hazard of any specific conductor is difficult to predict. Furthermore, the high bandwidth required for present day's ultrasound imaging is hardly compatible with the several meters of ultra-thin and high-loss coaxial cables necessary to keep the catheter design practical.

To overcome these challenges, fiber optics have been proposed to replace metal wires [12], for example inside an active position-tracking system for catheters [13]. Glass or plastic optical fibers show low magnetic susceptibility and are immune to RF interference, allowing low-noise imaging during electro-physiologic interventions. As opposed to state-of-the-art research and striving for the highest possible level of integration, we desire to replace all conductors in an ICE catheter by a single optical fiber, therefore electrifying the device with light, and setting the path for a smarter and cost effective generation of catheters. This study reports on a fully functional bench-top demonstrator that is immediately scalable to catheter dimensions. Signal transfer of synthetic aperture ultrasound images using a VCSEL (vertical cavity surface emitting laser) and optical fiber is shown together with power transfer over optical fiber, which uses violet light and *receiving* gallium nitride LEDs (light emitting diodes) as biocompatible photo-voltaic converters [14, 15] to supply all electronics. In our proposed solution, the absence of conductors provides galvanic isolation as well as intrinsic RF and MRI compatibility and the simple design utilizing off the shelf components holds a promise of cost effectiveness all of which may help translation of these advanced devices into the clinic.

2. Materials and methods

2.1. Experimental system layout

The long term objective is to build an ICE catheter where all electrical wires will be replaced by fiber optics. The intermediate step towards this goal is to provide a scalable proof of concept. To this aim a bench-top setup consisting of a several blocks is built, as shown schematically in Fig. 1 and on a photograph in Fig. 2.

The left block, the interrogator console, contains laser sources to generate optical power and a custom ultrasound system which generates control signals. Electrical and optical connections are shown as solid and dashed arrows, respectively. The ultrasound system also performs beam-form processing of the received sensor signals, and the display shows the resulting ultrasound image.

The middle block depicts three optical fibers and a few electrical wires for transmission of the control signals connecting the left and right block. For the long term goal, one laser source with fiber can be replaced by a beam splitter at the catheter tip and the same fiber can be used as a return path using a dichroic mirror at both ends. Then, also the control signals will be sent over the same optical fiber and some receiving logic should be integrated in the catheter tip. Ultimately, only a single optical fiber will need to be integrated in the catheter shaft. This study compares system performance for electrical and optical connection and therefore the system is designed to allow replacing of the optical connections with electrical wires.

The right block comprises a capacitive micro-machined ultrasonic transducer (CMUT) array,

Optics EXPRESS

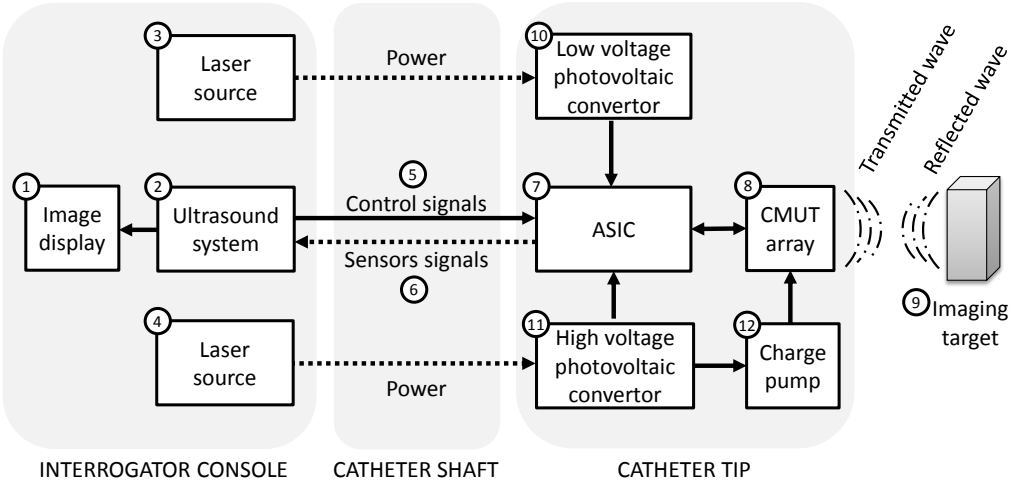

Fig. 1. Schematics of the opto-electrical ultrasound imaging system. Electrical connections are shown as solid arrows and the optical connections are shown as dashed arrows. For comparison of system performance, the optical connections can be replaced by electrical wires. The labelled numbers correspond to the components shown in a photograph in Fig. 2.

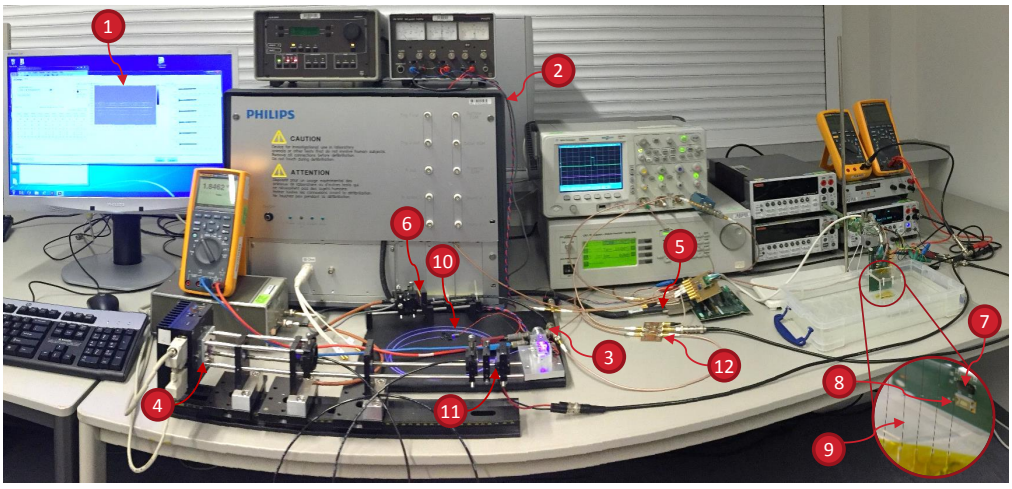

Fig. 2. Photograph of the opto-electrical ultrasound imaging system. The labelled numbers correspond to the items shown in a schematic drawing in Fig. 1.

Optics EXPRESS

an application specific integrated circuit (ASIC), low and high voltage photo-voltaic convertors, and a charge pump designed to be integrated in a catheter tip. The CMUT is immersed in water and utilized to both transmit an acoustic wave and receive the reflected echoes.

2.2. Transducer

The CMUT array is fabricated on 6-inch 670 μm thick silicon wafer utilizing a sacrificial release process [16–18]. The array consists of 512 active CMUT cells, each cell has a diameter of 60 μm at a separation distance of 63.6 μm. The cells are arranged in 16 array elements, each containing 32 cells aligned in one column. The total active area is $2 \times 1\ mm^2$. The top electrodes of each array element are wire-bonded via a printed circuit board (PCB) to the 16 channels of the ASIC. The bottom electrode is short circuit and connected to a common ground. The CMUT cells are operated in collapse-mode and require a magnitude of negative bias voltage higher than −65 V (typically −90 V) applied to the electrodes via 1 MΩ resistor. The surface of the CMUT is covered with approximately 15 μm thick layer of a silicon-like material for passivation and electrical insulation of the wirebonds. The CMUT array is mounted on the PCB without any acoustic backing layer.

2.3. ASIC

An already existing ASIC is used. It was designed to generate high voltage positive pulses to drive the CMUT cells, and it amplifies and buffers the received sensor signals. The ASIC is made by XFAB XP018 technology which provides high-voltage components based on 5 V gate-oxide transistors, that allow a maximum high-voltage swing of 60 V, which is additive to the negative bias voltage – see Fig. 3. The low-voltage transistors have a feature size of 0.18 μm and run at a typical supply voltage of 1.8 V.

Functionality of the ASIC is shown schematically in Fig. 3. The ASIC contains 16 transmitters that are capable of generating single-ended high-voltage pulses to stimulate the top electrodes of the CMUT array elements (the array columns). The ASIC also comprises 16 receivers for read-out of the elements. A multiplexer drives the low voltage stimulus signal to one of the high voltage transmitters. Another multiplexer connects one of the receivers to the signal output channel. A capacitor of 10 nF is used to decouple the high-frequency stimulus and echo-signals from the DC bias current. The amplified (26 dB) and buffered output signal is transferred from the ASIC to an ultrasound imaging system either via a 50 Ω coaxial cable or via an optical transmission link. This ASIC configuration allows generating synthetic aperture ultrasound images. The ASIC requires two external supply domains. A high-voltage supply domain which can be used at a range of 10 V – 60 V and a low-voltage supply domain of 1.8 V.

2.4. Electronic boards

The CMUT array and ASIC are mounted on a PCB, which hosts 47 nF and 100 nF capacitors connected to the common ground to stabilize the source voltage in the low and high voltage domains, respectively. The power to both voltage domains is provided via a pin header connector mounted on the PCB. Bias voltage, control signals, sensor signals are connected via a 0.5-m long cable and a JAE312 connector mounted on the PCB. The proximal end of the cable clicks on a fan-out board which connects 5 control signals (reset, TX control, RX control, TX/RX switch, transmit pulse) and the bias voltage via standard 50 Ω coaxial wires.

2.5. Ultrasound system

The control signals and the transmit pulse are generated by a custom high-frequency ultrasound imaging system (Philips Research, Eindhoven, the Netherlands) having a −6 dB bandwidth of 5 MHz – 50 MHz. The system is capable of driving the CMUT with arbitrary pulses defined by time increments of 5 ns. The 14-bit analogue-to-digital (AD) convertor sampling time is 5 ns.

Optics EXPRESS

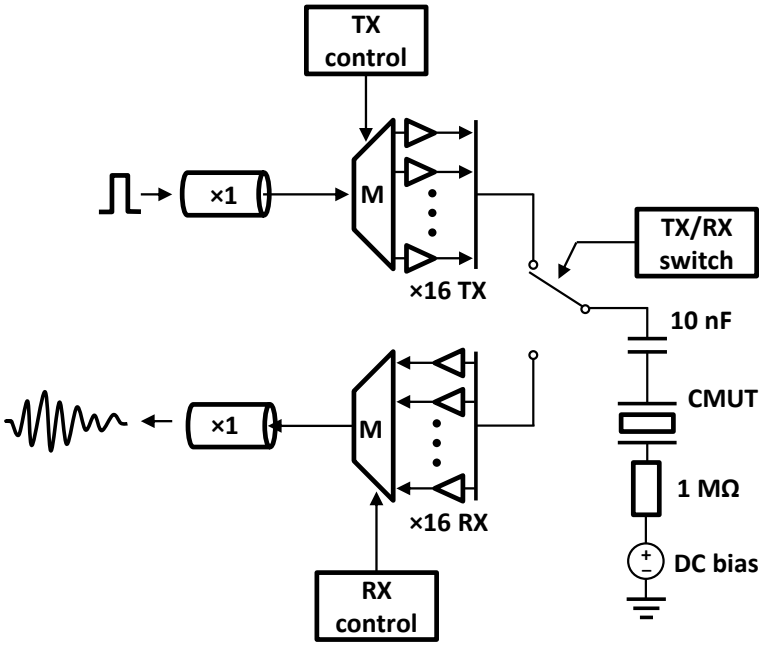

Fig. 3. Schematic diagram of the ASIC functionality. The ASIC consists of 16 high voltage transmitters (TX), 16 receivers (RX), two multiplexers (M) controlled by the transmit (TX) and receive (RX) control signals, and a transmit-receive (TX/RX) switch which connects the ASIC to the CMUT array.

The sensor signals from the CMUT array are compensated for attenuation by TGC, 16 times averaged and stored at a local hard-drive for off-line processing before being displayed.

2.6. Signal generation and data acquisition

The ASIC is controlled via 5 signals which are generated at the pulse repetition frequency (PRF) of 2 kHz. The repetition period is divided into a transmit and receive window which define one acquisition event. Typical length of the transmit window and receive window is 2048 and 8192 samples, respectively. In total 289 ($(16 + 1)^2$) acquisition events are generated in sequential order to acquire synthetic aperture data from all combinations of 16 individual physical and one "dummy" array element. During the dummy acquisition event, the transmit pulse is switched off and the receive remains active. A reset pulse is generated at start up, or once signals from all the elements have been received. The desired transmit and receive array element is selected by applying the TX control and RX control signals in cyclical order, ie. n consecutive pulses at the transmit multiplexer selects the n^{th} array element for transmit. After the appropriate elements are chosen, the transmit-receive control signal switches the ASIC chip to transmit mode and disconnects the receive circuitry to protect it from overvoltage generated by the high-voltage pulser. An arbitrary unipolar pulse (typically 1 – 2 periods of 12 – 14 MHz) is generated in the transmit mode and the transmit-receive control signal switches the ASIC back to the receive mode. A signal having a frequency of 16 kHz is generated to seed the high-voltage bias needed for the CMUT array and will be discussed later in Sec. 2.10. All control signals are synchronized with a 200 MHz clock of the ultrasound system and have an amplitude of 1.8 V.

Optics EXPRESS

2.7. Image processing

A total of 289 signals are recorded, out of which 256 signals contain the ultrasound echo signal, 16 signals from the dummy transmit element are subtracted from the signals received by the corresponding element to compensate for various artifacts (e.g. unwanted echo generated by switching in between transmit and receive modes). The remaining 17 signals from the dummy receive element are not used. A synthetic transmit aperture method is utilized to form the ultrasound images [19]. A 90° sector image is defined in a polar grid with an angular resolution of 5° and radial resolution of half the acoustic wavelength. The received signals are band-pass filtered with a linear-phase finite impulse response digital filter at a center frequency of 12 MHz and bandwidth of 6 MHz. A Hilbert transformation and a Hanning-window apodization is applied to the received signals. A beamforming algorithm finds the instantaneous envelope of the received signals at pre-defined grid points to form a low resolution image. When the width of the array element is comparable to the wavelength corresponding to the center frequency of the transmitted signal, angular dependence of the element's sensitivity has to be taken into the account by applying weights to the received signals [20]. The weights are estimated by the means of a single element directivity function,

$$f(\Theta) = \frac{sin(\pi d/\lambda sin\Theta)}{\pi d/\lambda sin\Theta} cos\Theta, \tag{1}$$

where d is the element width and Θ is the observation angle. This is repeated for all 16 transmissions. The low resolution images are coherently added to form one high resolution image. The absolute value of the high resolution image is then visualized in a 40 dB range.

2.8. Optical signal transmission

To transfer signals from the ASIC to the ultrasound system analog modulation is applied to the vertical-cavity surface-emitting laser (VCSEL) emitting at 850 nm (ULM850-10-TT-C0104U, ULM Photonics, Ulm, Germany). The laser current is modulated in amplitude by the pre-amplified ultrasound signal via the 4.7 nF decoupling capacitor, and Fig. 4 shows that the P-I characteristic of the laser is linear above threshold ($I_{th} \approx 1$ mA). Note that the I-V characteristic of the laser shown in Fig. 4 indicate that, above threshold, it has a (differential) impedance of approximately 50 Ω. As indicated in the electronic layout in Fig. 5, the effective impedance seen by the ultrasound signal is 34 Ω due to the necessary 300 Ω and 110 Ω resistors, of which the first one sets the DC bias current for the VCSEL and the latter one is required to eliminate charge build up at the ASIC's output circuit.

The modulated optical signal is focused by a lens on a photodiode (S5972, Hamamatsu, Hamamatsu City, Japan), amplified by a 20 dB amplifier (HP8447A, Hewlet-Packard, Palo Alto, CA, USA) which is connected to the ultrasound system. The electronic layout of the optical receiver is shown in Fig. 6. An impedance analyzer (HP8753ES, Hewlet-Packard, Palo Alto, CA, USA) is used to measure the total available bandwidth of the optical signal transmission.

2.9. Low voltage optical power

A single blue LED, type Luxeon Z Royal Blue (Philips Lumiled, San Jose, CA, USA), is used perhaps counterintuitively not as a light source but as a photovoltaic convertor to power both the low-voltage domain of the ASIC as well as to bias the VCSEL used for the optical signal transmission. The current-voltage characteristics of the LED can be found in [21]. This LED is illuminated by light from a (HD-DVD or Blu-ray disc) laser (OEM) at a wavelength of 405 nm. The light from the laser is coupled via a lens and dichroic mirror (DLMP425, Thorlabs Inc, Newton, NJ, USA) into a 400-μm thick glass optical fiber (FT-400-UMT, 3M, St. Paul, MN, USA) which is in direct contact with the Luxeon Z LED. The dichroic mirror alows observing the Photo-Induced Electro Luminescence (PEL) from the LED which provides a measure for

Optics EXPRESS

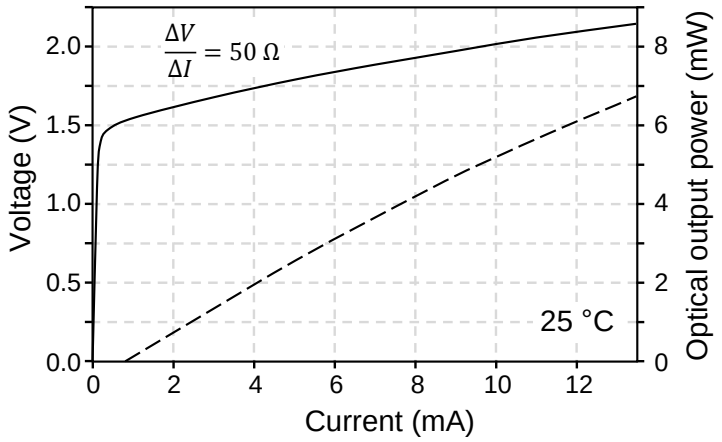

Fig. 4. VCSEL characteristics: the current-voltage (solid) and current-power (dashed) curves.

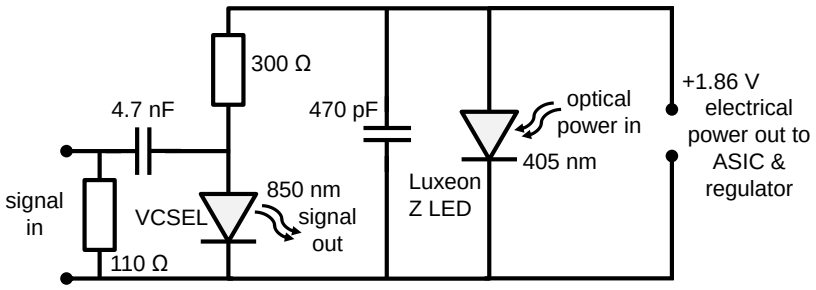

Fig. 5. Electronic layout of the optical transmitter connected to the optical low voltage power supply.

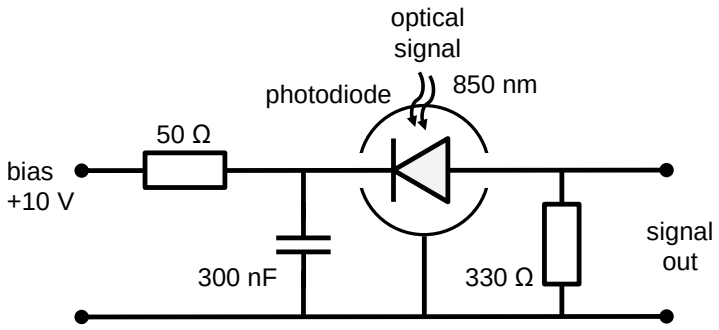

Fig. 6. Electronic layout of the optical receiver.

Optics EXPRESS

the resistive load on the LED by the electronics. The PEL signal may be used as a feedback signal to optimize the laser power [22]. The optical power on the LED has been measured with a photodiode (S2386-8K, Hamamatsu, Hamamatsu City, Japan). The VCSEL is powered from the LED via the 300 Ω resistor which sets the DC bias current sufficiently above laser threshold. The measured VCSEL's bias voltage is 1.56 V.

The same LED is connected in parallel to a shunt regulator (ZR431LF01TA, Zetex, Oldham, United Kingdom) which limits the maximum current to 50 mA and stabilizes the output voltage to 1.8 V to protect the ASIC's sensitive low-voltage domain. This part has been added to protect the electronics from transients or overload while experimenting and may be omitted when a final design is implemented in the catheter tip. A wire connects the stabilized low-voltage to the PCB with the ASIC.

2.10. High voltage optical power

The Luxeon H, a 50 Volt multi-LED chip (Philips Lumiled, San Jose, CA, USA) consists of 18 monolithically integrated LEDs in series and is used as a photovoltaic convertor to power the ASIC's high voltage domain [21]. The bare chip is illuminated by a high power violet laser diode (NDV7375E, Nichia, Tokushima, Japan). The light from the laser is coupled into a 1-mm thick glass optical fiber (FT-1.0-URT, 3M, St. Paul, MN, USA) via a lens and then through a $1.5 \times 1.5\,\mathrm{mm}^2$, 25-mm long glass mixing rod directly on the Luxeon H chip. In this way, the $1.5 \times 1.5\,\mathrm{mm}^2$ area of the segmented LED is illuminated homogeneously and each of the segments can deliver the same current. The optical power on the Luxeon H chip has been measured with a photodiode (S2386-8K, Hamamatsu, Hamamatsu City, Japan). A coaxial wire is used to connect the Luxeon H chip to the high voltage domain of the ASIC and to the input of the charge pump. The PRF of 2 kHz and the duration of 2 periods of a 14 MHz pulse results in a duty cycle of 0.3 ‰. Considering a 5 mW average power consumed by the ASIC pulser results in a peak power of 17.5 W. Such a peak power cannot be delivered instantaneously by the optical link. However, the calculated energy required for the pulse generation is only 2.5 µJ. This amount of energy can be stored in a 2.6 nF capacitor charged at 44 V. To account for an over-head, a 100 nF capacitor is used in the ASIC's high voltage domain to store the charge required for the generation of the transmitted pulses.

The charge pump is applied to invert and boost up the input voltage above the level required to collapse the CMUT cells (about −90 V). It utilizes the 16 kHz switch signal to charge the capacitors connected in series with the source to approximately double the input voltage. Output of the charge pump is connected to the fan-out board and then via the cable to the CMUT array.

2.11. Frequency response and image characteristics

The CMUT array is characterized in a pulse-echo experiment. Center frequency and −6 dB bandwidth of the received echo are measured per array element. Synthetic aperture ultrasound images of a wire and a tissue-mimicking cyst phantom are acquired. In both experiments, the CMUT array is connected to the optical power and signal link and, alternatively, to the conventional electrical power and signal link at the same input source voltages. The signals received with the optical and electrical power and signal link are compared. The generated images of the two phantoms are evaluated by comparison to simulations done using the Field II package [23, 24]. The images are characterized by commonly used contrast-to-noise ratio (CNR) and image signal-to-noise ratio (SNR) calculated using the following equations [25]:

$$\mathrm{CNR} = \frac{|\mu_\mathrm{i} - \mu_\mathrm{o}|}{\sqrt{\sigma_\mathrm{i}^2 + \sigma_\mathrm{o}^2}}, \tag{2}$$

Optics EXPRESS

where μ_i and μ_o are the mean signals at the same depth inside and outside the phantom feature, respectively. σ_i and σ_o are the standard deviations of signals at the same depth inside and outside the phantom feature, respectively.

$$\mathrm{SNR} = 20 \times \log_{10}\left(\frac{\mu_i}{\sigma_o}\right). \tag{3}$$

Note that the simulation takes into account only the signal generated noise neglecting any thermal or quantization noise effects [26].

3. Results

3.1. Power considerations

Table 1 shows the measured average power consumption. The ASIC consumes, on average, 30 mW of the input power, out of which 25 mW is continuous power needed for the receive chain and 5 mW is used for generation of transmitted pulses. To account for the peak power demand of the ASIC pulser the 100 nF capacitor in the ASIC's high voltage domain is continuously recharged via the high voltage optical power link and partially discharged during the pulse generation. The low voltage ASIC domain does not exhibit any peak power demands and is therefore continuously powered by the low voltage optical link. Table 2 summarizes the measured efficiencies of the low and high voltage optical links.

Table 1. **Average electrical power consumption by electronics.**

		Voltage (V)	Current (mA)	Power (mW)
High voltage	ASIC pulser	44	0.106	4.7
	CMUT bias	−88.5	0	0
	Charge pump (16 kHz)	44	0.211	9.3
Low voltage	ASIC logics and amplifiers	1.86	13.3	25
	Low voltage stabilizer	1.86	1	1.9
	VCSEL	1.56	1	1.56
Total power requirements				42.5

Table 2. **Optical power link efficiency.**

	Electrical power into laser (mW)	Optical power on LED (mW)	Electrical power from LED (mW)	Conversion efficiency (%)
Low voltage	595	77.4	28.5	36.8
High voltage	1407	104.5	14	13.4

3.2. Signal characteristics

The bandwidth of the optical signal link is measured to be 200 MHz as shown in Fig. 7. The signal was filtered down to 30 MHz bandwidth to be compatible (to prevent folding) with the AD-conversion in the ultrasound receiver.

Typical pulse-echo waveforms, received by a single array element, from a wire target using the optical or electrical version of the imaging setup are compared in Fig. 8a. Center frequency and bandwidth of individual transducer elements for the two versions of the setup are shown in Fig. 8b and Fig. 8c, respectively.

Optics EXPRESS

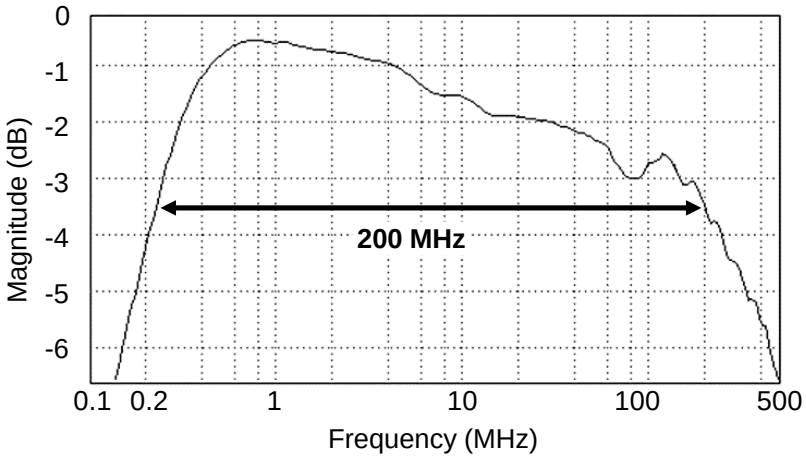

Fig. 7. Optical signal link bandwidth.

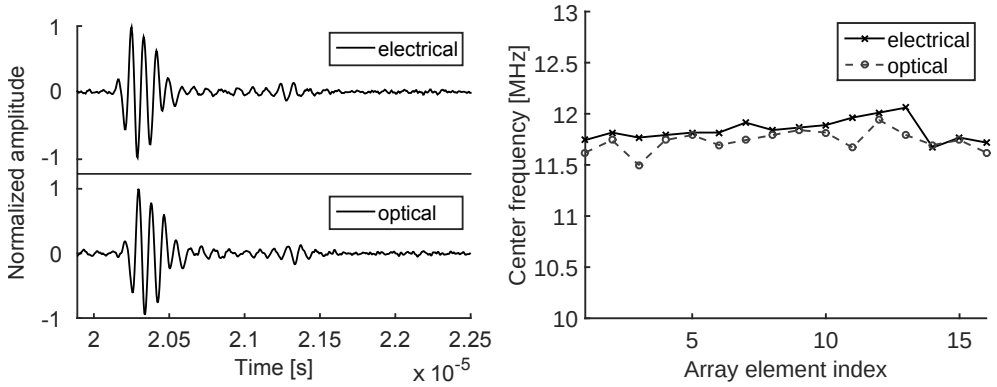

(a) Waveforms

(b) Center frequency

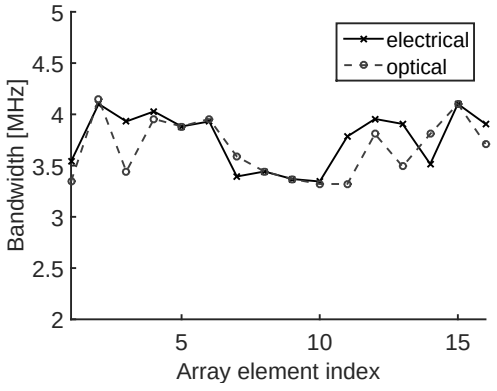

(c) Bandwidth

Fig. 8. Typical pulse-echo transducer array characteristics.

Optics EXPRESS

3.3. Imaging

Figure 9a shows a simulated synthetic aperture ultrasound image of a wire phantom generated with the designed CMUT array. The simulation is compared to images of a custom-made wire phantom obtained experimentally using the optical power and signal link, and to its electrical equivalent as shown in Fig. 9e and Fig. 9c, respectively. Similarly, Figs. 9b, 9d and 9f compare images of a cyst phantom. Quantitative image characteristics are summarized in Table 3.

Table 3. Image characteristics

	Target	Figure	CNR (-)	SNR (dB)
Simulation	wire	9a	0.5	67
Electrical link	wire	9c	0.5	50
Optical link	wire	9e	0.5	35
Simulation	cyst	9b	1.9	23
Electrical link	cyst	9d	1.6	22
Optical link	cyst	9f	1.6	22

4. Discussion

As shown in Fig. 8a, no significant difference is observed between the waveforms acquired via the conventional electrical and the novel optical link. The array uniformity in center frequency and bandwidth is shown in Figs. 8b and 8c, respectively. The frequency responses of the individual array elements are uniform. No significant differences in resonance frequency or bandwidth are observed between the CMUT powered and read-out via the optical fibers as compared to the conventional electrical wires.

Lateral resolution in the experimental images of the wire phantom (Figs. 9c and 9e) matches well with the simulation shown in Fig. 9a. As compared to the simulation, axial resolution in the experimental image is compromised due to the ringing in the silicon substrate of the fabricated CMUT [27]. No difference in resolution is observed between the CMUT connected to the optical power and signal link as compared to the electrical wires.

Table 3 summarizes the characteristics of all obtained images. The experimentally obtained image of the wire phantom (Fig. 9c) shows 17 dB lower SNR as compared to the simulation (Fig. 9a). This is because the simulation takes into account only the signal generated noise neglecting the thermal and quantization noise, which decreases the SNR in the experimental image. The image acquired with the optical link has SNR of 35 dB, which is ample for ultrasound imaging as barely any difference is observed in comparison of the images shown in Figs. 9c,(e). Although the CNR definition in Eq. (2) is a commonly used image quality metric [25] to expresses the fact that detectability increases with increasing object contrast and decreasing acoustic noise, its numerical value is highly object dependent. Therefore the CNRs of all the three images of the wire phantom are equal to a relatively low value of 0.5 as compared to the CNRs of a cyst phantom.

Figure 9b shows a simulated image of the cyst phantom exhibiting a contrast-to-noise ratio of 1.9 and SNR of 23 dB. These values are comparable to those of B-mode image of a cyst presented in the literature [25]. The experimental image generated with the electrical link (Fig. 9d) shows 0.3 lower contrast-to-noise ratio and only 1 dB lower SNR than the simulation, indicating that the SNR is dominated by the signal generated noise rather then thermal or quantization noise. The dynamic range of the optical link as compared to the electrical one is very much the same as demonstrated by the identical CNR and SNR values of 1.6 and 22 dB, respectively measured in the images of the cyst phantom (Figs. 9d,(f)). The experimentally obtained dynamic range of 22 dB is remarkable, given the small size of the aperture ($1 \times 2\,\mathrm{mm}^2$) and the chosen synthetic

Optics EXPRESS

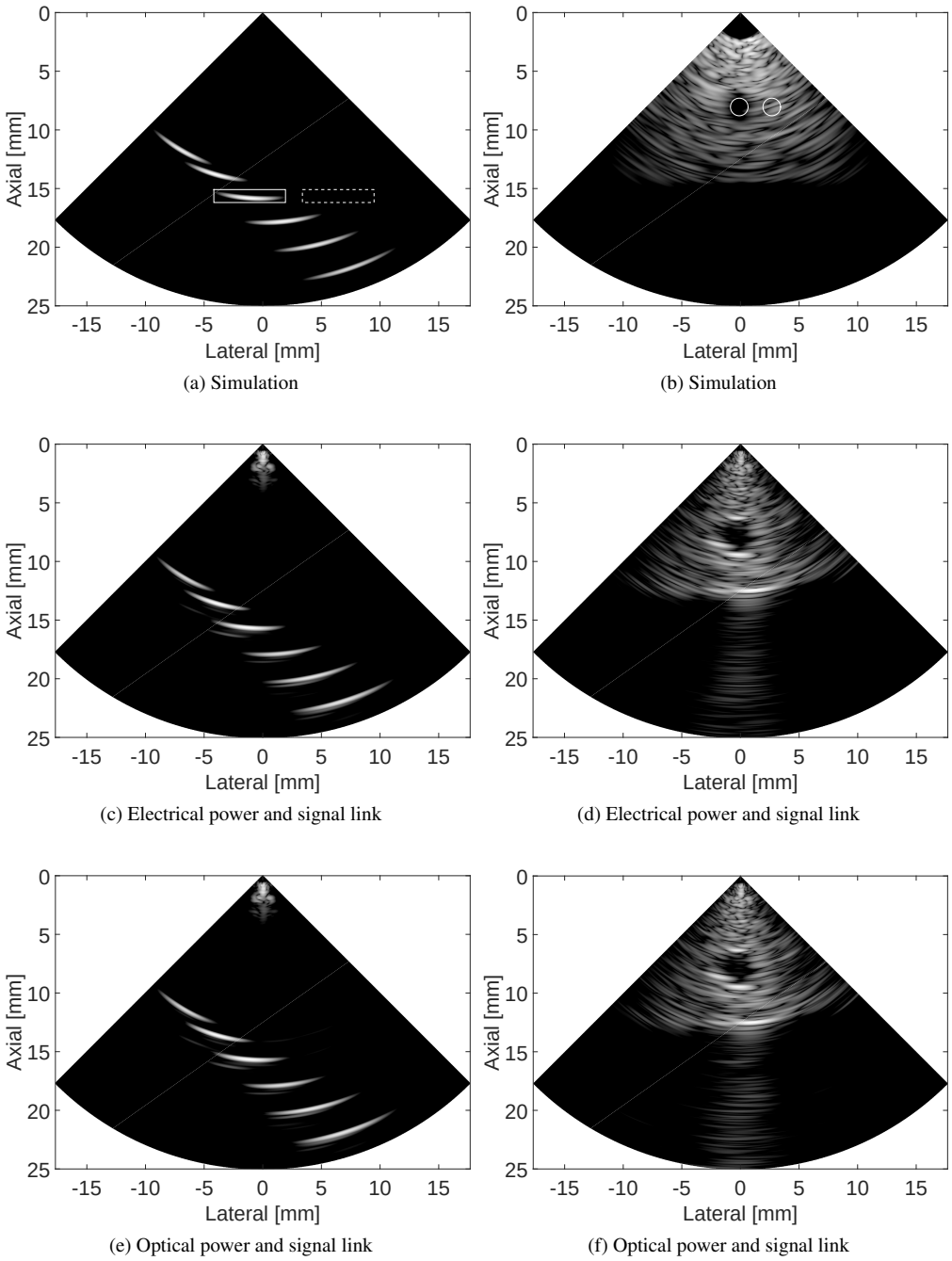

(a) Simulation (b) Simulation

(c) Electrical power and signal link (d) Electrical power and signal link

(e) Optical power and signal link (f) Optical power and signal link

Fig. 9. Synthetic aperture images of (a, c, e) a wire phantom and (b, d, f) a cyst phantom shown at a dynamic range of 40 dB. The white (a, c, e) rectangles and (b, d, f) circles show the region of interest inside (solid) and outside (dashed) the phantom feature used for the calculation of the image characteristics (CNR, SNR).

Optics EXPRESS

aperture imaging method when only a single element is used in transmit and receive mode. A chirp technique or multi-element synthetic aperture imaging could be employed to further increase the SNR to the value of 40 dB typically used in medical ultrasound imaging [19, 28].

Note that the darkening of the sector images at large angles of the cyst phantom happens due to the low element's angular sensitivity, which is a projection of its area in the given direction, a cosine of the angle, for both transmission and reception.

A reception bandwidth of 200 MHz of the ultrasound signals is achieved by utilizing amplitude modulation of a VCSEL (Fig. 7) and non-linear distortion is avoided by operating the VCSEL in its linear regime. The optical signal transfer does not suffer from RF-signal interference in comparison to poorly-shielded thin coaxial wires as would be the case for integration of wires in a catheter.

The optoelectronic components presented in this study will ultimately have to fit in a catheter tip and must show sufficiently low heat dissipation so that they will not harm or denature adjacent tissue or passing blood. The presented photovoltaic-conversion dissipates 139 mW of electrical power (Table 2). The reverse conversion efficiency of the low voltage LED reaches 37 % which is close to the limit of its design efficiency. The high voltage LED's efficiency is 13 %, which can be improved up to about 25 % by more homogeneous illumination of the 18 LEDs on the Luxeon H chip. The conversion efficiency can be further increased by matching the voltage requirements of the ASIC and the CMUT array to the limits of the LEDs, putting them in a more favorable working point. Also the charge pump presented here is rather inefficient and its current can be lowered by at least a factor of 10 (unpublished observation). The low voltage power dissipation of 25 mW from the ASIC is relatively high because all 16 receiver amplifiers are powered in the receive mode. This power could be lowered by factor of 16 when the ASIC is optimized for receiving with only a single amplifier. Similarly, the high voltage power dissipation can be reduced by powering only a single transmitter. Despite the possibility for optimization of the system efficiency, the amount of power dissipated in the small contact area is sufficiently low for intracardiac catheters placed typically in the flowing blood pool of the heart. Optimization will allow reaching the limit for intravascular catheters (100 mW for a catheter of 1.8 mm in diameter [29]), which have four times smaller cross-sectional area and are placed in tight coronary arteries. Then it is also possible to irrigate the catheter to lower its temperature, or a heat conducting element in the catheter tip may spread the heat load and reduce the temperature.

The reason for using a GaN device, the blue LED, as a photovoltaic convertor is its high bandgap of 2.8 eV which provides a compact power source that can deliver directly up to 2.4 V. In addition to that, the LED device can handle high power density on the order of 1 W/mm^2, which is at least hundred times more than that of a silicon photodiode. Using the high power-density LED enables the optical solution presented in this study to be integrated in an intra cardiac catheter having a typical diameter of about 3 mm.

Previous demonstration of light powering in a magnetic resonance catheter detector utilized a GaAs photovoltaic convertor [13]. The disadvantage of GaAs is, however, its toxicity and a low bandgap (1.1 eV), which results in a factor of two lower power density as compared to GaN. Our approach, which utilizes a non-toxic GaN LED is therefore a more appropriate solution for medical devices, in which the biocompatibility and power density is of crucial importance.

All the components have been designed with a catheter-scale miniaturization in mind. The Luxeon Z and Luxeon H chip having the package dimensions of $1.0 \times 1.0\,\mathrm{mm}^2$ and $1.6 \times 1.6\,\mathrm{mm}^2$, respectively, exhibit a great power density allowing its integration in a tip of an intracardiac catheter. Using a different wavelength for optical power delivery and signal transmission enables single-optical fiber integration, some of which designs have been published earlier [21]. Nevertheless, the integration challenge of the individual optical components (ie. beam splitters, lenses) needs to be solved before the all-optical ICE imaging catheter can be built.

Optics EXPRESS

An ICE catheter is a single-use device, of which the price exceeds a few thousand Euro. Lowering the costs is therefore critical so that patients may benefit from these medical devices. Batch manufacturing possibility of CMUT, low price of the optical components, and the simple synthetic aperture ultrasound imaging technique will enable development of a low-cost ICE system [30–33].

The minimum time to receive echoes from a depth of 31.5 mm is 41 μs resulting in a maximum PRF of 24 kHz. Such a system would allow imaging at 83 FPS without averaging. Due to the limited bandwidth of the data stream channel the system presented in this paper achieves maximum PRF of 2 kHz, which results in a very slow frame rate considering the 16 times averaging. Therefore only images of static objects were acquired.

The presented device facilitates five low voltage control signals for the ASIC which is at odds with the all-optical concept. Re-design of the ASIC is needed to transmit all the control signals in series via a single channel. These control signals could then be transmitted via an optical signal link analogue to the one presented in this paper. Such a device would facilitate solely optical connections between the distal sensor and proximal end, thus providing total galvanic isolation (therefore eliminating the need and desire of grounding the catheter tip), immunity to RF interference, MRI compatibility and safety.

The current design utilizes a shunt regulator to limit the maximum current and to stabilize the output voltage to protect the ASIC's sensitive low-voltage domain during the various experiments. This regulator can, however be omitted once all the design parameters are optimized and fixed, increasing the efficiency of the optical power transmission and decreasing the size of the device.

The practical data rate of a VCSEL transmitter is 10 Gb/s which is large enough to transmit, in parallel, 16 AD-converted ultrasound signals with 40 dB dynamic range, therefore speeding up the acquisition and limiting the required number of connections within the restricted space of a catheter. To this aim of full frame imaging, the development of a small-size and low power AD-converter would be required. The measured bandwidth of the VCSEL-based optical link described in this paper is 200 MHz, which is limited by the rather bulky passive components used to match the impedance of the VCSEL to set its operating point and by the bandwidth of the amplifier connected to the photodiode. It should be noted that in our electronic design no coils or ferrites have been used anywhere and that this was done to make sure that the ultimate goal, of total miniaturization and integration in a catheter, can be met.

5. Conclusion

We have built a bench-top demonstrator that is scalable to catheter dimensions, in which conventional electrical wires used for ultrasound sensor-signal and power transfer are replaced by three optical fibers. We have shown photo-voltaic conversion of 405 nm light to 44 V and 1.8 V by two blue LEDs to supply all electronics. Synthetic aperture ultrasound images were acquired at a frequency of 12 MHz with a collapse-mode CMUT. Analog modulation of a 850 nm VCSEL showed 200 MHz broad-band signal transfer. System bandwidth, noise level and dynamic range are nearly identical as shown in comparison of the images acquired with the optical link and its electrical equivalent. The absence of conductors will provide galvanic isolation and intrinsic RF / MRI compatibility without any noticeable loss in the image quality. The robust and simple design holds a promise of cost effectiveness and facilitates the emerging application of (bi-directional) photo-voltaic devices with fiber-optics as a backbone of connectivity in medical catheters. These results may assist translation of such advanced devices into the clinic.

Funding

European Union Seventh Framework Programme (EU FP7) (317526); Electronic Components and Systems for European Leadership Joint Undertaking (ECSEL JU) (2014-2-662155).

Optics EXPRESS

Acknowledgments

The authors would like to thank the following people for their effort and support: Anneke van Dusschoten, Alfons Groenland, Nenad Mihajlović, Walter Hermans, John Reuvers, Jim Oostveen and Peter Barendse.